GOALS: The Great Observatory All-sky LIRG Survey
First Data Delivery
Jan 2008

1. Introduction

This document describes the first data delivery of the Spitzer Legacy program, GOALS. The Great Observatory All-sky LIRG Survey (GOALS) combines imaging and spectroscopic data from NASA's Spitzer, Hubble, Chandra and GALEX observatories in a comprehensive survey of over 200 of the most luminous infrared-selected galaxies in the local Universe (see http://goals.ipac.caltech.edu). This delivery contains imaging (IRAC and MIPS) and spectroscopic (IRS) data for 50 galaxies in the GOALS sample. This document is organized as follows: section 2 lists the data products, their general characteristics and naming convention, sections 3, 4, and 5 provide a description of the post-BCD processing for IRAC, MIPS and IRS data, respectively, and section 6 presents derived data and diagnostic diagrams (e.g. derived fluxes, spatial profiles, etc.) associated with the Spitzer data.

2. Content of the data delivery

The 50 galaxies included in this first delivery were selected from the complete GOALS sample, including only those systems for which we have obtained IRS spectra at the time of delivery. Table 1 lists the galaxies with images and spectra in this delivery. The following is a list of data products:

- IRAC image mosaics at 3.6, 4.5, 5.6 and 8μm. All images are single-extension FITS files. The pixel scale of the mosaics are 0.6 arcsec, and the flux (surface brightness) units are MJy/sr. The mosaics have standard orientation with North up and East to the left.
- MIPS image mosaics at 24, 70, and 160 microns. All images are single-extension FITS files. The pixel scale of the mosaics are wavelength dependent: 1.8 arcsec at 24μm, 4.0 arcsec at 70μm, and 8.0 arcsec at 160μm. The flux (surface brightness) units in all cases are MJy/sr. The mosaics have standard orientation with North up and East to the left.
- IRS nuclear spectra in the Short-Low, Long-Low, Short-High and Long-High modules. IRS spectra are delivered in ASCII (*.tbl) format, similar to those produced by the IRS pipeline. The flux units are Jy.
- Spatial profiles at two positions along the IRS SL slit, in the 8.6 μm PAH, 10 μm continuum, and 12.8 μm [NeII] fine-structure emission line. Profiles are provided in ASCII format, in unitis of e^{-1}/sec listed for each spatial pixel. Also included in each file are the profiles at the same three wavelengths for an unresolved standard star. Figure 5 shows an example of the spatial profile at one nod position for the galaxy NGC 5653. The files are structured as follows:

Col. 1: Spatial pixel
Col. 2: Median flux per pixel at 12.8 μm for SL 1st order, nod 1
Col. 3: Same as col. 2, but for the calibration star
Col. 4: Median flux per pixel at 10 μm for SL 1st order, nod 1
Col. 5: Same as col. 4, but for the calibration star
Col. 6: Median flux per pixel at 8.6 μm for SL 1st order, nod 1
Col. 7: Same as col. 6, but for the calibration star
Col. 8-13: Identical to col. 2-7 but for SL 1st order, 2nd nod position

2.1 File Naming Convention

For each galaxy, the delivered Spitzer data have the following filename conventions:

- **IRAC mosaics**: NAME_irac_chN.fits, where NAME is the object name and N is the channel number (1 = 3.6 μm, 2 = 4.5 μm, 3 = 5.8 μm, and 4 = 8 μm)
- **MIPS mosaics**: NAME_mips_chN.fits, where NAME is the object name and N is the channel number (1 = 24 μm, 2 = 70 μm, and 3 = 160 μm)
- **IRS spectra**: NAME_chN.tbl, where NAME is the object name and N is the channel number (0 = SL, 1 = SH, 2 = LL, 3 = LH)
- **IRS spatial profiles**: NAME_SP.dat_dr1, where NAME is the object name, SP indicates it is a spatial profile, and _dr1 stands for delivery 1.

Table 1: GOALS Sources in delivery #1

Galaxy	Log L_{IR}	RA (J2000)	DEC (J2000)
ESO353-G020	11.0	01h34m51.26s	-36d08m14.4s
NGC3221	11.0	10h22m19.98s	+21d34m10.6s
ESO432-IG006	11.02	08h44m27.21s	-31d41m50.8s
ESO432-IG006_2		08h44m28.93s	-31d41m30.3s
NGC0992	11.02	02h37m25.46s	+21d06m02.8s
NGC6907	11.03	20h25m06.58s	-24d48m32.9s
NGC0877	11.04	02h17m59.68s	+14d32m38.2s
NGC0877_2		02h17m53.26s	+14d31m18.4s
UGC11041	11.04	17h54m51.82s	+34d46m34.2s
NGC6701	11.05	18h43m12.52s	+60d39m11.6s
IRAS04271+3849	11.06	04h30m33.09s	+38d55m47.8s
NGC5653	11.06	14h30m10.44s	+31d12m55.8s
NGC5990	11.06	15h46m16.41s	+02d24m55.6s
NGC5936	11.07	15h30m00.85s	+12d59m22.1s
UGC01845	11.07	02h24m07.97s	+47d58m11.9s
IC4280	11.08	13h32m53.40s	-24d12m25.5s
CGCG468-002	11.1	05h08m19.71s	+17d21m47.8s
CGCG468-002_2		05h08m21.21s	+17d22m08.0s

NGC0317B	11.11	00h57m40.41s	+43d47m32.5s
MCG-05-12-006	11.12	04h52m04.96s	-32d59m26.0s
ESO286-G035	11.13	21h04m11.11s	-43d35m36.1s
CGCG465-012	11.15	03h54m07.67s	+15d59m24.3s
CGCG465-012_2		03h54m15.95s	+15d55m43.4s
IRASF06592-6313	11.17	06h59m40.26s	-63d17m52.4s
ESO267-G030	11.19	12h14m12.81s	-47d13m42.5s
ESO267-G030_2		12h13m52.28s	-47d16m25.4s
IRAS05083+2441	11.21	05h11m25.88s	+24d45m18.2s
UGC03351	11.22	05h45m48.03s	+58d42m03.6s
MCG-03-34-064	11.24	13h22m24.45s	-16d43m42.4s
IRAS05442+1732	11.25	05h47m11.20s	+17d33m46.4s
IRASF03217+4022	11.28	03h25m05.37s	+40d33m32.2s
IC4734	11.3	18h38m25.75s	-57d29m25.4s
ESO138-G027	11.34	17h26m43.35s	-59d55m55.2s
UGC03608	11.3	06h57m34.41s	+46d24m10.6s
IRAS13052-5711	11.34	13h08m18.73s	-57d27m30.3s
ESO264-G036	11.35	10h43m07.51s	-46d12m44.1s
UGC02608	11.35	03h15m01.47s	+42d02m08.6s
UGC02608_2		03h15m14.58s	+41d58m50.0s
IRAS05129+5128	11.36	05h16m55.96s	+51d31m56.9s
IRAS03582+6012	11.37	04h02m32.99s	+60d20m41.8s
IRAS03582+6012_2		04h02m31.97s	+60d20m38.3s
MCG+08-11-002	11.41	05h40m43.70s	+49d41m41.6s
ESO507-G070	11.49	13h02m52.42s	-23d55m17.8s
IRAS23436+5257	11.51	23h46m05.44s	+53d14m01.7s
IRAS08355-4944	11.56	08h37m01.87s	-49d54m30.0s
IRAS18090+0130	11.58	18h11m38.42s	+01d31m40.3s
IRAS18090+0130_2		18h11m33.41s	+01d31m42.4s
IRAS12116-5615	11.59	12h14m22.08s	-56d32m32.7s
IRASF06076-2139	11.59	06h09m45.74s	-21d40m24.5s
UGC02369	11.6	02h54m01.84s	+14d58m15.7s
VV340a	11.67	14h57m00.70s	+24d37m05.8s
VV340a_2		14h57m00.32s	+24d36m24.6s
IRAS21101+5810	11.75	21h11m29.28s	+58d23m07.9s
ESO239-IG002	11.78	22h49m39.84s	-48d50m58.3s
IRASF18293-3413	11.81	18h32m41.10s	-34d11m27.0s
CGCG448-020	11.87	20h57m24.09s	+17d07m35.2s
CGCG448-020_2		20h57m24.38s	+17d07m39.2s
ESO069-IG006	11.92	16h38m11.85s	-68d26m08.2s
IRASF09111-1007	12.0	09h13m36.50s	-10d19m29.7s
IRASF09111-1007_2		09h13m38.89s	-10d19m19.6s
IRAS07251-0248	12.32	07h27m37.62s	-02d54m54.8s

Table 1. GOALS sources included in this delivery: Object name is given in Col.1, infrared luminosity (log L_{IR} in units of $L_{\odot}$) is given in Col.2, and RA and DEC (J2000) are given in Cols. 3 & 4, respectively. Note, that L_{IR} is only listed for the first galaxy in multiple-galaxy systems, since this is measured for the entire system.

3. IRAC Data Processing

Initial steps of the IRAC data reduction were provided by Version S11 of the Spitzer Science Center (SSC) pipeline. Further processing was performed using a combination of IDL and IRAF routines. Detector artifacts in the IRAC data include "banding," "muxbleed," and "column pulldown," as described in the IRAC Data Handbook (2006). Several steps were taken to improve upon the Basic Calibrated Data (BCD) from the SSC pipeline. First, instrumental artifacts were removed. The 3.6 and 4.5 μm images suffer from muxbleed and pulldown affecting the rows and columns (respectively) that contain cosmic ray hits, bright stars, or bright galactic nuclei. The 5.8 and 8.0μm images often have banding artifacts extending along the rows containing galactic nuclei or other bright features. IDL routines developed by the IRAC Instrument Support Team were used to correct all three types of artifact. However, residuals from these correction techniques remain in the final images, especially residual banding at 8μm. The first frame of the 5.8μm data was always excluded due to excessively high background levels compared to the other frames. For each field containing the target galaxy or interacting system, individual BCD images were spatially aligned, resampled, and combined into a mosaic image. The SSC Post-BCD software package MOPEX was used for the alignment and resampling, and to mask out known bad pixels in each band. The IRAF module imcombine was used to make mosaics using the images output by MOPEX. Cosmic ray artifacts were removed by sigma-clipping when the mosaics were constructed. In some cases, most often in the 5.8μm mosaics, background mismatches between BCD images were corrected using the overlap script within the MOPEX package. Although overlap effectively removes background variations between adjacent images, large-scale gradients over a mosaic are preserved. The overlap routine also provides an alternative means of cosmic ray removal.

Due to the presence of bright galactic nuclei, we utilized the high dynamic range (HDR) mode in all four bands. The HDR frames are comprised of 1-2 sec exposures ("short" integration) to calibrate pixels that would have saturated in the 30-second exposures ("long" integrations). Data presented here are mosaics of the long integrations where such mosaics are not saturated. In the event of saturation (very rare for ch1-3, common for ch4), short exposure mosaics are used instead. The EXPTIME header keyword indicates which type of mosaic has been provided.

For each mosaic, the background level has been measured and subtracted from the image. This value is recorded in the BACKGROU header keyword.

4. MIPS Data Processing

4.1. *The 24 μm Si:As Detector Array*

The BCD pipeline products from the 24 μm channel of MIPS contain some artifacts, mostly due to very bright flux densities, for many of the sources in our program (see

Table 1). Notable features in the Si:As (IBC) array data are bright latent image spots trailing along the in-scan direction from bright sources (very rare), and in some cases dark latents (1-2% depressions in responsivity) for sources brighter than about 18 Jy. Residual gradients in the background from the pipeline flat-fielding process are also present at the 1-2% level in many of the 24 μm images. A weak "jail-bars" effect is often present in the BCDs, reflecting different readout gains rather than saturation. Another potential problem is optical distortion at 24 μm, which can induce photometric calibration variations of 2-10% across the array in some frames; the post-BCD pipeline reductions correct for this particular problem using MOPEX. More detailed descriptions and illustrations of these instrumental effects are given in the MIPS Data Handbook (2006). Where possible, the self-calibration procedure (self-cal) was used to remove latents and weak jailbars. However, often the small number of input images (14, for the most common AOR) precluded self-calibration. The overlap routine discussed in §3, which is part of the MOPEX package, was used in the initial stages of mosaic creation at 24μm. The final mosaics, after treatment for saturation effects where present (§§4.3), were constructed using the mosaic routine of MOPEX.

4.2. *The 70 and 160μm Ge:Ga Detector Arrays*

MOPEX was used to resample and align the MIPS BCD images and combine them while rejecting pixels flagged as suffering from latent image artifacts. The 70μm BCD images were filtered using column filter and time filter IDL routines created by D. Fadda. These routines offer an improvement over the filtered BCD images generated by the pipeline by masking the position of the target(s) prior to filtering. MOPEX was used to align, resample, and combine the filtered MIPS images into final mosaics in all three MIPS bands.

For each mosaic (ch1-3), the background level has been measured and subtracted from the image. This value is recorded in the BACKGROU header keyword. Note that the filtering procedure used on the ch2 data removes most of the background, resulting in the very small, sometimes negative BACKGROU values recorded for those mosaics.

4.3. *Treatment of MIPS Saturation Problems*

The bright galactic nuclei in our sample presented saturation problems for many of the MIPS observations. The saturation limits for a 1-second observation of a point source are approximately 4 Jy, 18 Jy, and 3 Jy at 24, 70, and 160μm, respectively. At 24μm, a strong "jailbar" pattern with depressed responsivity in every fourth column appears around saturated sources; bright 24μm sources may also saturate parts of the array, resulting in a DC offset that thwarts the pipeline's default "droop correction" algorithm. Individual frames displaying these saturation problems were removed prior to the creation of the final mosaic with MOPEX using the remaining frames that did not display indications of saturation. The typical pattern in the data was several saturated images (strong jailbars) followed by useful, unsaturated data frames.

At 70 and 160μm, the Spitzer MIPS Ge Reprocessing Tools (GeRT) package was utilized

to correct the BCDs for saturation problems. To fix saturated pixels, the GeRT mosaic was matched to the initial MOPEX mosaic by computing their ratio and scaling the GeRT mosaic appropriately. A pixel mask was then applied, and the missing pixel(s) from the GeRT mosaic were used to produce a corrected MOPEX mosaic. The GeRT was configured to require a minimum of two data samples to estimate the slope of the signal. Severely saturated images, which are saturated on the first or second point of the integration ramp, could not be recovered with the GeRT, and are thus unusable for photometry.

4.3.1 Saturated Galaxies

There were two galaxies in this delivery with saturated MIPS channel 3 (160μm) data. These are UGC 03351 and IRASF18293-3413.

5. IRS Data Processing

Dedicated sky observations were used for sky subtraction of the high resolution IRS data. For the low resolution spectra, off-source nods were used for sky subtraction, unless dedicated sky observations were available. B-mask files were combined such that bmask_final[i,j]=max(bmask_N[i,j]) where i,j are the pixel coordinates and the bmask_Ns are the bmasks corresponding to each bcd in both the nod and the data used for sky subtraction. BCDs and "func" files for each nod were combined (median for N>5, average with 3-sigma clipping otherwise) as well.

Each nod was extracted with SPICE using the standard extraction aperture, and point-source calibration. Nod-1 and nod-2 were compared with each other, with pixels flagged if the difference between nod1 and nod2 exceeded 10%, and when adjacent pixels within the same nod differed by >10% (i.e., from a cosmic ray or hot pixel). Flagged pixels were excluded when the nods were combined into the final spectrum for each object. Order matching was performed on SL data. SL3 (the "bonus order") was scaled to match SL1, then SL2 was scaled to match SL3. A sample spectrum of NGC6701 is shown in Fig. 1.

5.1 Notes on individual objects

Order mis-matches are sometimes seen in the IRS LH data. The IRS Instrument Support Team at the SSC is actively working towards a solution of this problem. Order mismatches are seen in the following objects: CGCG448-020_2, CGCG465-012, CGCG465-012_2, CGCG468-002_2, ESO267-G030_2, ESO432-IG006_2, IRAS03582+6012, IRAS13052-5711, IRAS18090+0130_2, and VV340a_2.

Spectral fringing is visible in the IRS LL spectra of the following objects: CGCG448-020_2, ESO264-G036, ESO432-IG006_2, IC4280, IRAS03582+6012, IRAS03582+6012_2, IRAS05442+1732, IRAS23436+5257, IRASF03217+4022, IRASF18293-3413, NGC0992, NGC3221, NGC5936, UGC02369.

The companion galaxy UGC02608_2 was observed in cluster mode with UGC02608 using the same exposure times for each galaxy. As a result, UGC02608_2 yielded only a very low S/N high-resolution IRS spectrum.

5.2 Photometric comparisons

IRS flux densities were calculated over the IRAC ch4 (8 μm) passband and the MIPS ch1 (24 μm) passband. Boxes corresponding to the extraction aperture for the relevant spectrum (SL for IRAC 8 μm, LL or LH for MIPS 24 μm) were used to measure the corresponding flux densities from the imaging data. These measurements are compared in Table 2 and Figs. 2-4. The offset seen between MIPS and both LL and LH is consistent with the offset seen between MIPS 24 μm and IRAS 25 μm: f (24μm MIPS) = (0.80±0.16) f (24μm IRAS intrp) where f (24μm IRAS intrp) is the IRAS flux density interpolated to the wavelength of MIPS ch1. Self-consistent color corrections using the full SED are expected to bring MIPS 24 μm measurements into consistency with IRAS and IRS (Lord 2008, private communication).

5.3 Spatial Profiles

Spatial profiles at three wavelengths in SL have been measured for all galaxies from the BCDs that were used in the SPICE extractions. The selected wavelengths are meant to isolate three features, namely the 8.6μm PAH, 10μm continuum, and 12.8μm [NeII] fine-structure emission line. Note, however, that the [NeII] profile can include significant flux from the 12.7μm PAH feature in addition to the fine-structure line. These are not easily separable without careful profile fitting in IRS low-res data. In all cases the profiles (e^{-1}/sec versus the pixel number in the X (spatial) direction across the processed 2D spectra) are median values over 5 pixels (in wavelength), and they are centered on the given feature in the observed frame. In SL, 1 pixel = 1.8 arcsec. Profiles for both nod positions are given in the delivered files. Example profiles, where we have averaged the nods and smoothed the profiles with a 1.5 pixel FWHM Gaussian, are shown below for NGC 5653 (see Figs. 5-7). This source is clearly resolved in all three spectral features. The ratio of the integrated flux in the source along the slit, to that of the standard star, at the observed wavelengths of 12.8, 10, and 8.6μm ($\mathcal{R}_{12.8}$, $\mathcal{R}_{10'}$ $\mathcal{R}_{8.6'}$), is given in Table 2 below. These ratios were obtained by dividing by the peak flux and then averaging the individual profiles at the two nod positions.

6. Derived Photometric Quantities

Table 2: Instrument Photometric Comparisons and IRS Spatial Profiles

Galaxy	IRS SL (Jy)	IRAC-8 (Jy)	IRS-LL (Jy)	MIPS-24 (Jy)	IRS-LH (Jy)	MIPS-24 (Jy)	$\mathcal{R}_{12.8}$	$\mathcal{R}_{10}$	$\mathcal{R}_{8.6}$
ESO353-G020	0.163	0.161	0.592	0.449	0.531	0.435	1.3	1.5	1.3
NGC3221	0.051	0.051	0.281	0.254	0.237	0.224	2.4	3.4	3.7
ESO432-IG006	0.108	0.112	0.417	0.333	0.400	0.324	1.3	1.3	1.3
ESO432-IG006_2	0.062	0.058	0.447	0.346	0.425	0.339	1.0	1.1	1.1
NGC0992	0.189	0.187	0.809	0.687	0.943	0.795	2.0	2.4	2.3
NGC6907	0.097	0.103	0.649	0.555	0.590	0.505	1.7	2.0	2.0
NGC0877	0.039	0.038	0.186	0.140	0.177	0.144	4.4	4.4	5.4
NGC0877_2	0.024	0.026	0.190	0.186	0.136	0.132	1.1	1.4	1.0
UGC11041	0.105	0.114	0.543	0.448	0.477	0.405	1.5	1.7	1.7
NGC6701	0.156	0.148	0.896	0.762	0.792	0.634	1.2	1.4	1.4
IRAS04271+3849	0.145	0.140	0.730	0.560	0.666	0.545	1.3	1.5	1.4
NGC5653	0.089	0.097	0.901	0.757	0.514	0.440	2.6	2.9	3.0
NGC5990	0.206	0.172	1.144	0.973	1.029	0.895	1.1	1.2	1.3
NGC5936	0.161	0.149	0.924	0.790	0.876	0.755	1.1	1.2	1.3
UGC01845	0.276	0.278	0.929	0.759	0.924	0.761	1.3	1.6	1.5
IC4280	0.081	0.083	0.342	0.299	0.288	0.260	2.4	3.0	2.9
CGCG468-002	0.069	0.073	0.362	0.298	0.341	0.282	1.0	1.0	1.0
CGCG468-002_2	0.082	0.079	0.773	0.604	0.734	0.601	1.1	1.4	1.3
NGC0317B	0.153	0.143	0.956	0.751	0.875	0.743	1.0	1.2	1.0
MCG-05-12-006	0.119	0.113	1.149	0.956	1.079	0.920	1.0	1.0	1.0
ESO286-G035	0.162	0.157	0.684	0.536	0.707	0.561	1.5	1.8	1.7
CGCG465-012	0.092	0.094	0.626	0.506	0.607	0.519	1.4	1.6	1.6
CGCG465-012_2	0.033	0.036	0.115	0.096	0.100	0.084	2.2	2.4	2.3
IRASF06592-6313	0.092	0.081	0.772	0.602	0.713	0.596	1.0	1.0	1.0
ESO267-G030	0.105	0.098	0.691	0.551	0.610	0.508	1.5	1.5	1.7
ESO267-G030_2	0.117	0.128	0.567	0.452	0.540	0.441	1.1	1.1	1.1
IRAS05083+2441	0.171	0.165	0.800	0.646	0.783	0.633	1.2	1.4	1.3
UGC03351	0.194	0.188	0.504	0.420	0.531	0.455	1.9	3.0	2.7
MCG-03-34-064	0.388	0.336	2.525	1.848	2.430	1.862	0.9	0.9	0.9
IRAS05442+1732	0.212	0.207	1.533	1.267	1.459	1.227	1.1	1.2	1.2
IRASF03217+4022	0.111	0.114	0.728	0.598	0.738	0.595	1.2	1.3	1.4
IC4734	0.146	0.151	1.117	0.876	1.004	0.825	1.1	1.3	1.2
UGC3608	0.086	0.082	0.985	0.757	0.945	0.798	1.1	1.3	1.5
ESO138-G027	0.109	0.106	1.131	0.874	1.041	0.868	1.1	1.2	1.3
IRAS13052-5711	0.083	0.079	0.349	0.257	0.313	0.262	1.2	1.5	1.3
ESO264-G036	0.069	0.086	0.365	0.319	0.415	0.359	1.7	2.0	2.0
UGC02608	0.174	0.161	1.338	1.050	1.180	0.998	1.0	1.0	1.1
UGC02608_2	0.006	0.007	0.033	0.028	0.037	0.023	2.1	2.3	2.6

IRAS05129+5128	0.099	0.094	0.846	0.669	0.793	0.656	1.1	1.2	1.2
IRAS03582+6012	0.243	0.199	0.566	0.460	0.520	0.393	1.0	1.4	0.9
IRAS03582+6012_2	0.060	0.059	0.575	0.449	0.527	0.417	1.3	1.5	1.5
MCG+08-11-002	0.226	0.216	0.858	0.634	0.787	0.628	1.1	1.5	1.1
ESO507-G070	0.112	0.101	0.771	0.570	0.707	0.560	1.0	1.1	1.0
IRAS23436+5257	0.058	0.065	0.572	0.478	0.545	0.469	1.1	1.2	1.2
IRAS08355-4944	0.234	0.203	2.025	1.696	1.943	1.663	1.0	0.9	1.0
IRAS18090+0130	0.128	0.127	0.535	0.412	0.522	0.422	1.3	1.7	1.6
IRAS18090+0130_2	0.024	0.024	0.155	0.115	0.147	0.111	1.1	1.3	1.2
IRAS12116-5615	0.218	0.201	1.140	0.875	1.056	0.879	1.0	1.0	1.0
IRASF06076-2139	0.053	0.053	0.595	0.440	0.537	0.429	0.9	1.1	0.9
UGC02369	0.106	0.126	1.201	0.985	1.204	0.991	1.2	1.2	1.4
VV340a	0.129	0.131	0.256	0.208	0.265	0.229	1.8	2.2	2.2
VV340a_2	0.023	0.022	0.071	0.057	0.067	0.056	2.7	3.8	3.4
IRAS21101+5810	0.065	0.059	0.592	0.457	0.556	0.452	0.9	1.0	1.0
ESO239-IG002	0.068	0.061	1.011	0.773	0.916	0.757	1.0	1.0	1.0
IRASF18293-3413	0.630	0.663	3.468	2.390	3.314	2.357	1.3	1.5	1.5
CGCG448-020	0.075	0.068	2.082	1.679	1.975	1.674	1.5	1.6	1.7
CGCG448-020_2	0.039	0.035	1.554	1.582	1.716	1.613	1.0	1.1	1.1
ESO069-IG006	0.207	0.199	0.637	0.491	0.587	0.483	1.2	1.5	1.4
IRASF09111-1007	0.052	0.052	0.331	0.252	0.301	0.247	1.0	1.3	1.1
IRASF09111-1007_2	0.033	0.033	0.179	0.142	0.169	0.141	1.1	1.2	1.3
IRAS07251-0248	0.045	0.038	0.564	0.401	0.507	0.391	0.9	1.0	0.8

Table 2 (above). Comparison of IRS, IRAC and MIPS Photometry: Derived fluxes for all the delivered sources. Col.2, IRS Short-Low flux density (in Jy) calculated over the IRAC 8μm filter bandpass. Col.3, IRAC 8μm flux density, derived from the imaging data, calculated over the projected area of the IRS Short-Low extraction aperture. Col. 4, IRS Long-Low flux density calculated over the MIPS 24μm filter bandpass. Col. 5, MIPS 24μm flux density, derived from the imaging data, calculated over the projected area of the IRS Long-Low extraction aperture. Col. 6, IRS Long-High flux density calculated over the MIPS 24μm filter bandpass. Col.7, MIPS 24μm flux density, derived from the imaging data, calculated over the projected area of the IRS Long-High extraction aperture. Col. 8-10, the ratio of the integrated normalized flux in the source along the slit, to that of the standard star, at the rest wavelengths of 12.8, 10, and 8.6 μm, respectively.

Table 3: Global IRAC and MIPS Photometry

Galaxy	IRAC-3.6 (Jy)	IRAC-4.5 (Jy)	IRAC–5.6 (Jy)	IRAC-8 (Jy)	MIPS-24 (Jy)	MIPS-70 (Jy)	MIPS-160 (Jy)
ESO353-G020	0.058	0.039	0.092	0.222	0.548	9.017	12.848
NGC3221	0.131	0.087	0.227	0.632	0.768	10.652	23.223
ESO432-IG006Sum					0.807	8.288	8.566
NGC0992	0.073	0.048	0.183	0.526	1.132	11.348	12.612
NGC6907	0.196	0.123	0.305	0.786	1.481	17.003	31.343
NGC0877	0.153	0.102	0.282	0.77	0.965	12.639	27.541
NGC0877	0.029	0.02	0.043	0.099	0.173	4.381	7.13
NGC6701	0.107	0.069	0.158	0.42	1.079	12.133	18.547
IRAS04271+3849	0.052	0.036	0.083	0.224	0.682	7.323	12.766
NGC5653	0.102	0.07	0.217	0.605	1.165	13.131	18.682
NGC5990	0.133	0.11	0.22	0.457	1.331	11.843	15.502
NGC5936	0.079	0.053	0.161	0.471	1.128	11.321	16.739
UGC01845	0.067	0.046	0.12	0.321	0.899	10.867	11.412
IC4280	0.08	0.052	0.141	0.4	0.529	7.389	13.718
CGCG468-002Sum	0.07	0.059	0.085	0.17	1.009	10.643	7.257
NGC0317BSum	0.115	0.081	0.104	0.19	0.872	9.489	10.458
MCG-05-12-006	0.03	0.021	0.035	0.115	1.06	8.173	7.365
ESO286-G035	0.044	0.03	0.102	0.296	0.715	9.162	10.406
CGCG465-012	0.025	0.017	0.038	0.135	0.177	2.28	5.518
CGCG465-012	0.062	0.042	0.098	0.225	0.647	6.316	8.833
IRASF06592-6313	0.024	0.016	0.036	0.082	0.691	6.371	4.852
ESO267-G030	0.09	0.061	0.124	0.291	0.56	6.937	10.608
ESO267-G030(ESO267-G029)	0.046	0.033	0.079	0.194	0.681	6.095	7.994
IRAS05083+2441Sum	0.036	0.025	0.077	0.223	0.79	7.127	7.315
UGC03351	0.098	0.065	0.185	0.494	0.736	17.253	
MCG-03-34-064	0.074	0.093	0.198	0.329	2.481	5.212	4.391
MCG-03-34-064	0.019	0.013	0.017	0.044	0.08	1.454	2.992
IRAS05442+1732	0.031	0.027	0.096	0.265	1.455	9.426	
IRAS05442+1732	0.017	0.011	0.025	0.069	0.096	1.338	
IRAS05442+1732Sum							10.172
IRASF03217+4022	0.089	0.069	0.083	0.16	0.709	8.033	6.373
IC4734	0.072	0.049	0.115	0.301	1.12	16.142	17.662
ESO138-G027	0.029	0.022	0.085	0.245	1.106	10.185	7.947
IRAS13052-5711	0.043	0.022	0.038	0.107	0.308	9.284	7.31
ESO264-G036	0.126	0.085	0.143	0.329	0.561	7.764	14.601
UGC02608	0.058	0.059	0.203	0.291	1.259	8.754	11.009
UGC02608	0.032	0.021	0.002	0.064	0.055	0.58	2.206
IRAS05129+5128	0.024	0.019	0.05	0.137	0.784	6.435	4.659
IRAS03582+6012Sum	0.038	0.066	0.225	0.273	0.576	5.953	5.236
MCG+08-11-002	0.051	0.039	0.098	0.283	0.754	15.869	17.071

ESO507-G070	0.037	0.026	0.047	0.112	0.656	13.816	10.248
IRAS23436+5257	0.022	0.019	0.035	0.077	0.604	6.09	3.63
IRAS08355-4944	0.048	0.056	0.124	0.244	1.9	8.843	2.895
IRAS08355-4944					1.914	8.781	3.849
IRAS18090+0130	0.043	0.03	0.075	0.216	0.526	7.958	
IRAS18090+0130	0.014	0.01	0.016	0.035	0.145	2.612	
IRAS18090+0130Sum							11.57
IRAS12116-5615	0.093	0.075	0.121	0.24	1.019	9.556	10.054
IRASF06076-2139Sum	0.018	0.013	0.02	0.058	0.529	6.657	5.406
UGC02369Sum	0.042	0.03	0.063	0.17	1.183	8.25	9.415
VV340aSum	0.056	0.042	0.1	0.312	0.433	9.381	15.728
IRAS21101+5810	0.041	0.027	0.033	0.069	0.543	6.896	9.227
ESO239-IG002	0.032	0.023	0.031	0.073	0.868	7.118	5.029
IRASF18293-3413	0.122	0.097	0.361	1.01	3.443	35.571	0
CGCG448-020Sum	0.022	0.021	0.05	0.151	2.05	11.701	6.482
ESO069-IG006	0.034	0.025	0.056	0.235	0.571	8.827	
ESO069-IG006	0.007	0.005	0.003	0.005	0.011	0.287	
ESO069-IG006Sum							10.138
IRASF09111-1007Sum	0.02	0.016	0.024	0.101	0.448	8.531	8.277
IRAS07251-0248	0.013	0.009	0.015	0.035	0.457	6.187	4.531

Table 3 (above). IRAC and MIPS Global Photometry: Total fluxes in IRAC and MIPS for the delivered sources. Cols. 2-5 are IRAC bands 1-4, respectively. Cols. 6-8 are MIPS bands 1-3, respectively. All entries are in Jy.

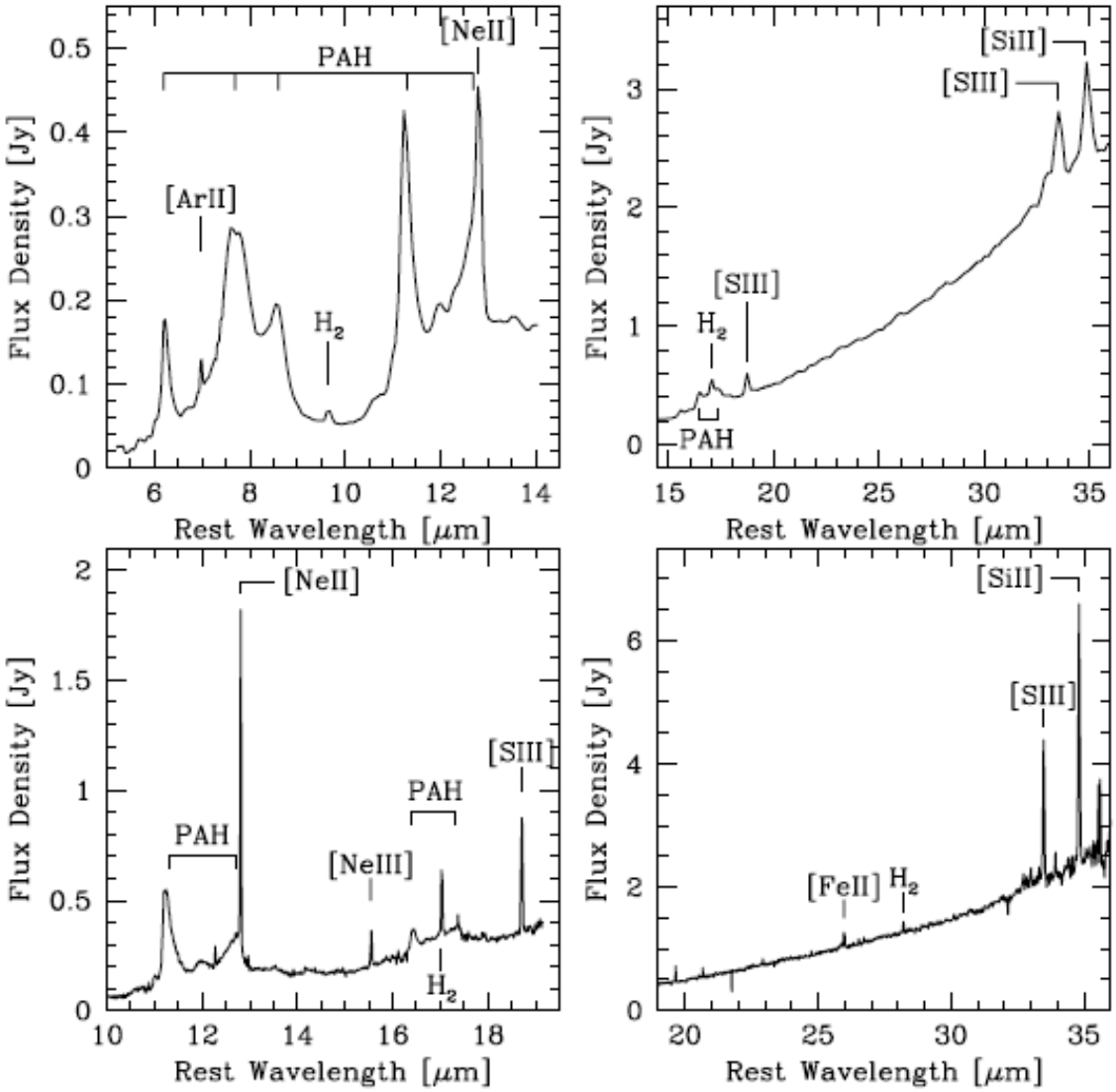

Fig. 1: IRS spectra of NGC6701. Short-low is in the top left panel, long-low in the top right, short-high in the bottom left, and long-high in the bottom right.

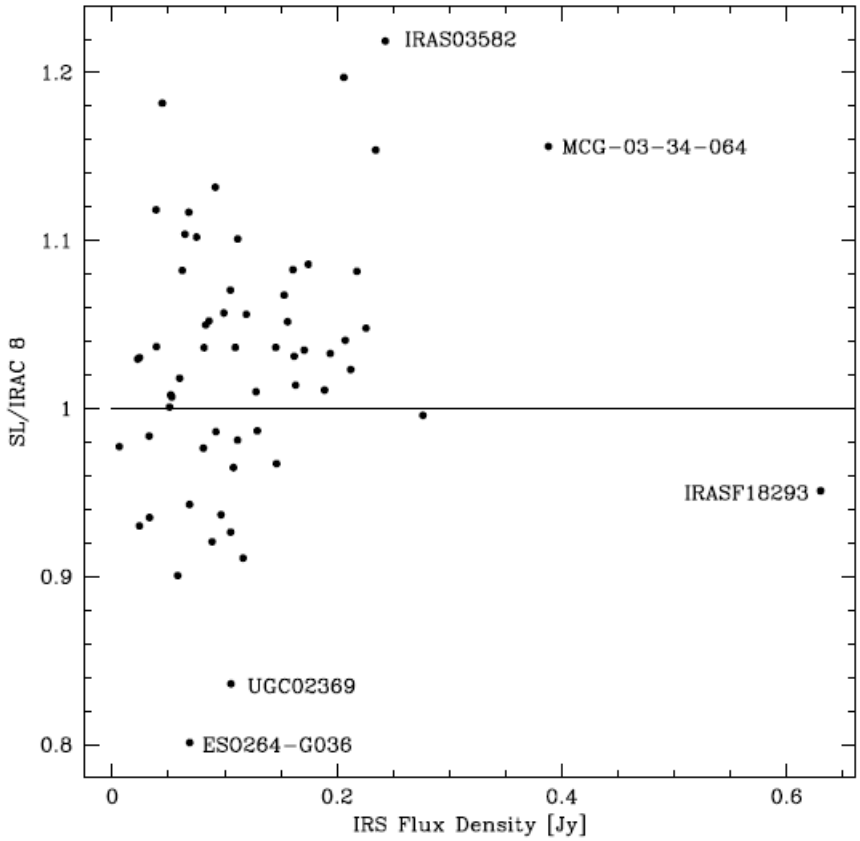

Fig. 2: IRS Short-Low 8μm flux density normalized by the IRAC band 4 (8μm) flux ratio vs. IRS Short-Low flux density. The IRS flux density is calculated over the IRAC 8μm filter bandpass. The IRAC flux density, derived from the imaging data, is calculated over the projected area of the Short-Low extraction aperture (an expanding aperture centered on the nucleus appropriate for a point source centered in the two-pixel wide slit), at the time of the observation. Outliers are labeled and discussed in the text. See Table 2 for derived fluxes.

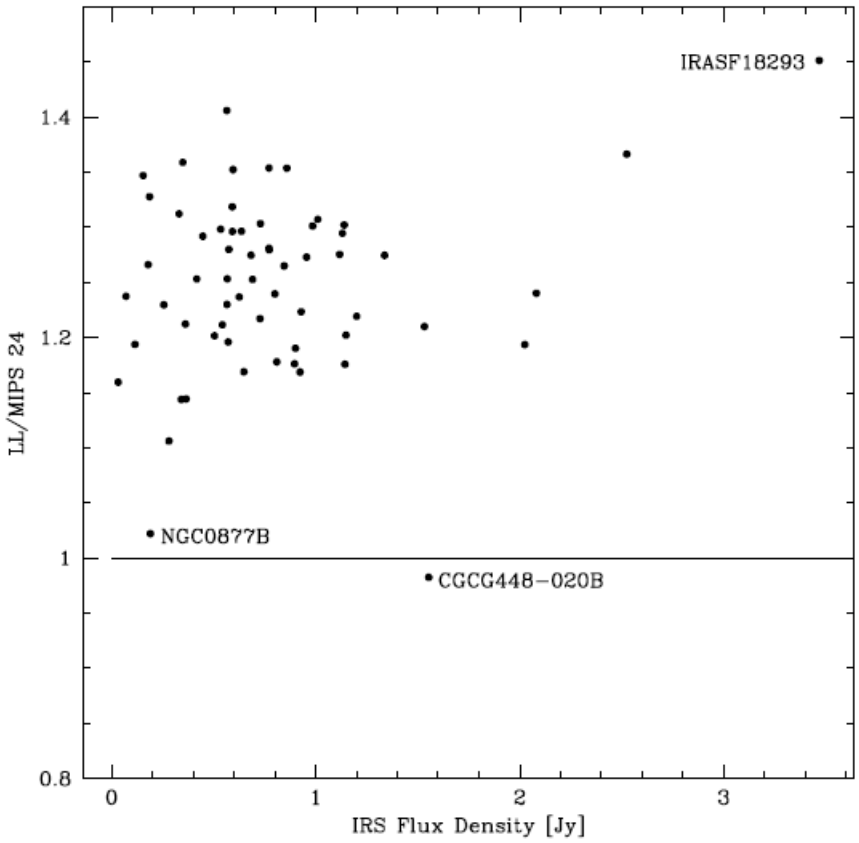

Fig. 3: IRS Long-Low 24μm flux density normalized by the MIPS 24μm flux ratio vs. IRS Long-Low flux density. The IRS flux density is calculated over the MIPS 24μm filter bandpass. The MIPS flux density, derived from the imaging data, is calculated over the projected area of the Long-Low extraction aperture (an expanding aperture centered on the nucleus appropriate for a point source centered in the two-pixel wide slit), at the time of the observation. Outliers are labeled and discussed in the text, as is the systematic 20-25% offset to higher LL/MIPS values. See Table 2 for derived fluxes.

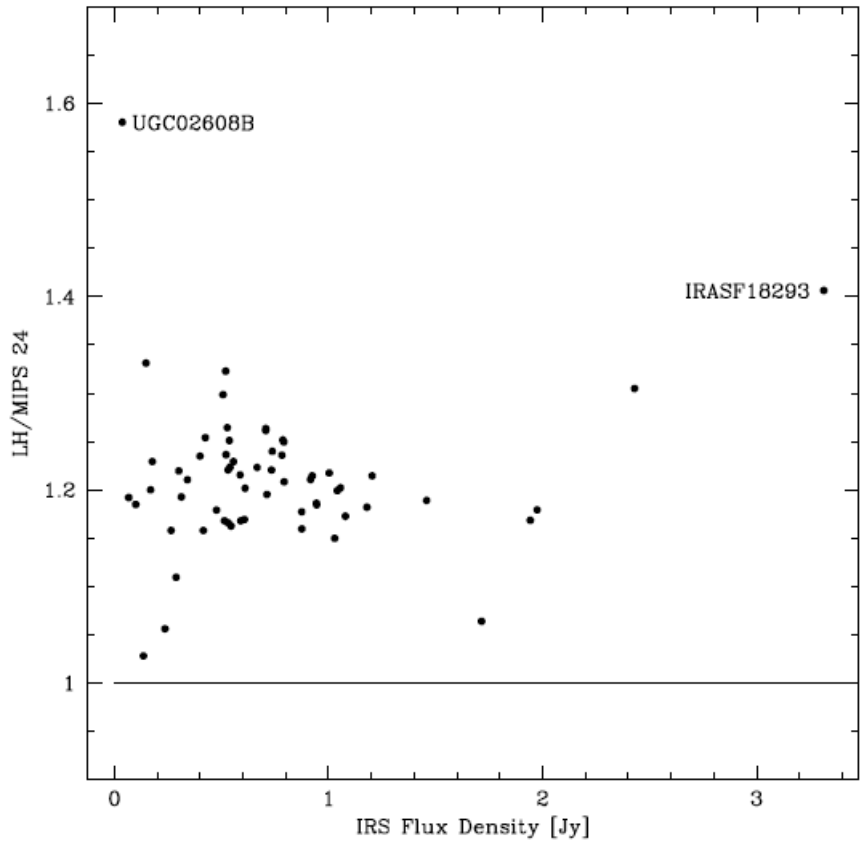

Fig. 4: IRS Long-High 24μm flux density normalized by the MIPS 24μm flux ratio vs. IRS Long-High flux density. The IRS flux density is calculated over the MIPS 24μm filter bandpass. The MIPS flux density, derived from the imaging data, is calculated over the projected area of the Long-High extraction aperture (an expanding aperture centered on the nucleus appropriate for a point source centered in the two-pixel wide slit), at the time of the observation. Outliers are labeled and discussed in the text, , as is the systematic 20-25% offset to higher LH/MIPS values. See Table 2 for derived fluxes.

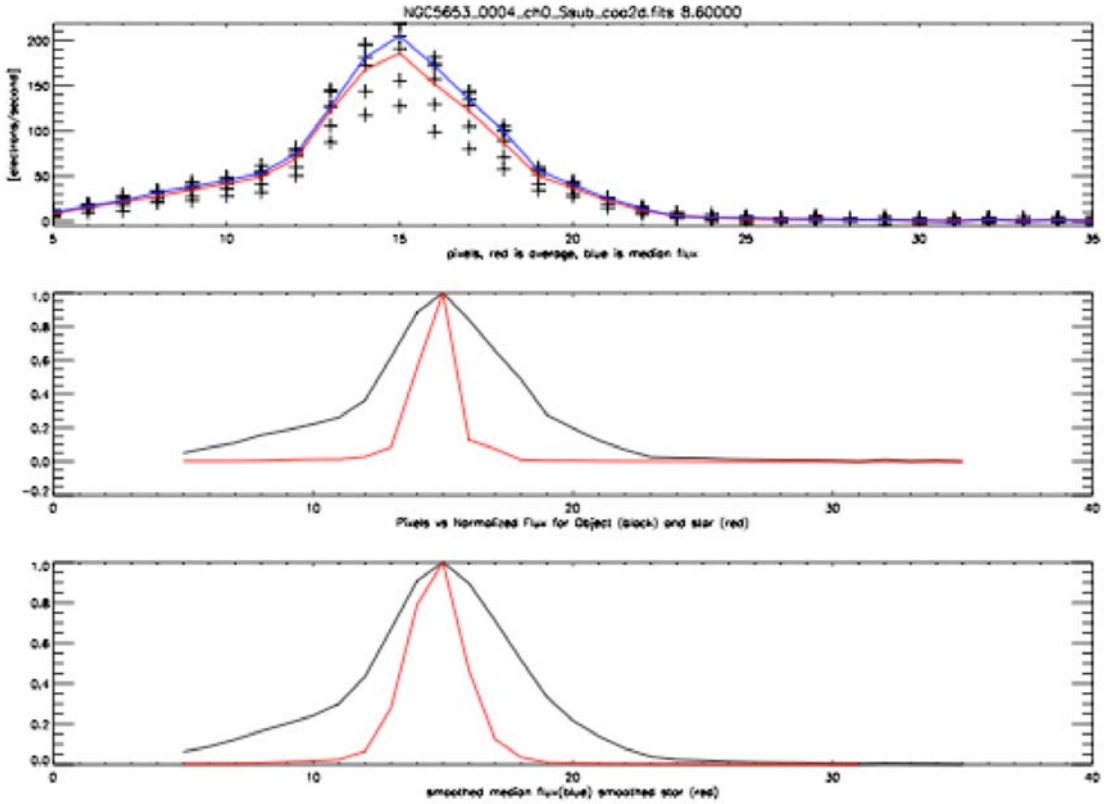

Fig. 5: Spatial profile of NGC 5653 along the IRS SL slit at a rest wavelength 8.6 μm (see text for details). The top panel shows the profile of the galaxy, along with the values for each of the five pixels centered at 8.6 μm (in the rest frame). The solid line is the median value at each pixel. The middle panel shows the profile of the galaxy (black) compared to that of a standard star (red) extracted in exactly the same manner, after aligning and normalizing to the peak surface brightness. In both cases the median value at each pixel is shown. In the bottom panel, both profiles have been smoothed with a Gaussian having a FWHM of 1.5 pixels.

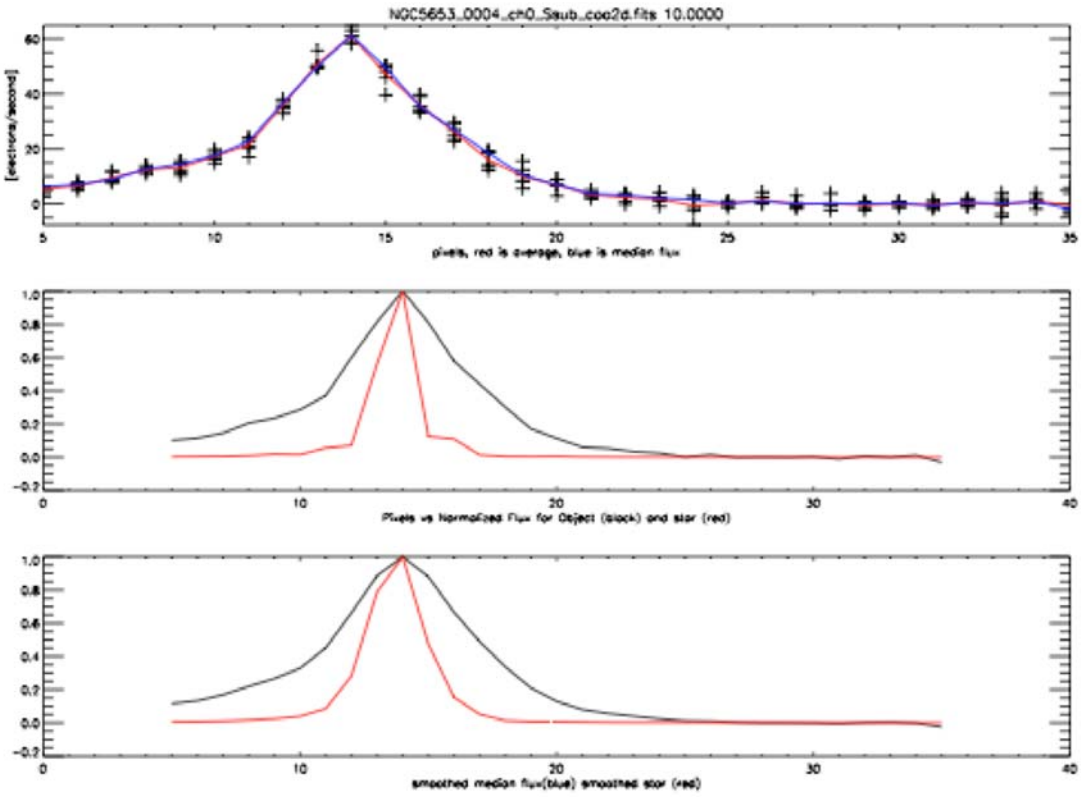

Fig. 6: Same as in Fig.5, but for the 10 μm dust continuum.

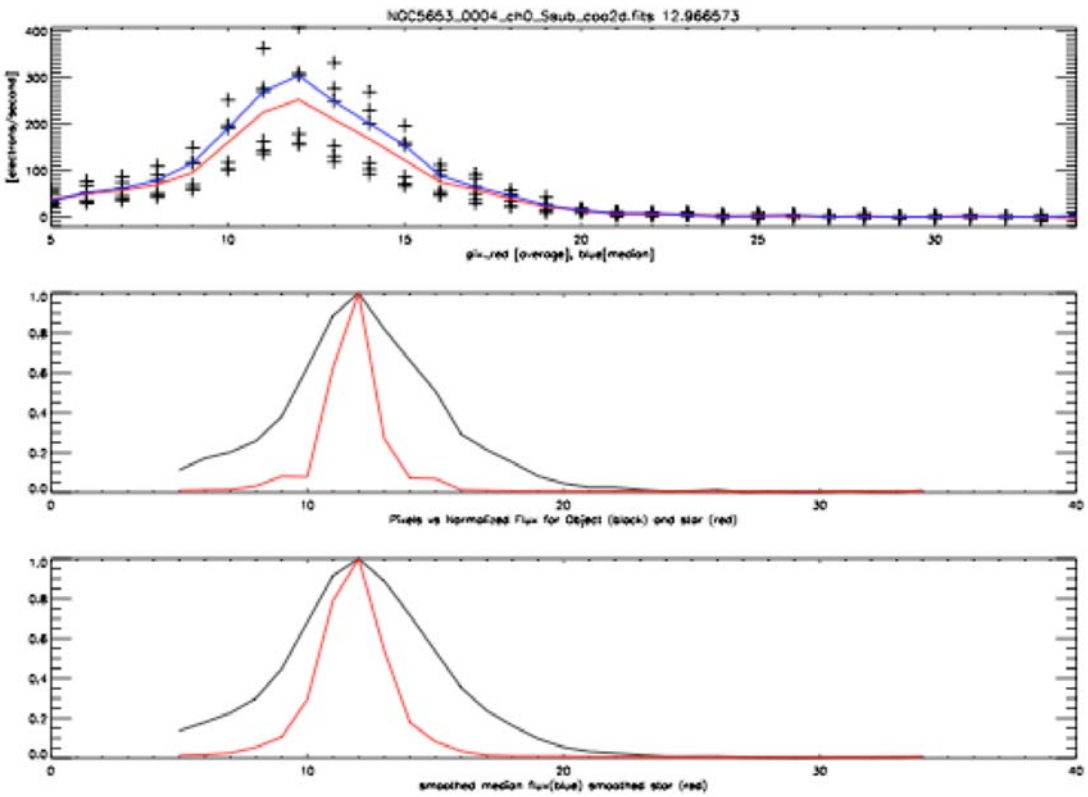

Fig. 7: Same as in Fig.5, but at a rest wavelength of 12.8 μm.